Florian Zimmermann*, Christoph Holst, Lasse Klingbeil, and Heiner Kuhlmann

Accurate georeferencing of TLS point clouds with short GNSS observation durations even under challenging measurement conditions

https://doi.org/10.1515/jag-2018-0013
Received April 10, 2018; accepted July 31, 2018

Abstract: The accuracy of georeferenced TLS point clouds is directly influenced by site-dependent GNSS effects, deteriorating the accuracy of the ground control point coordinate estimation. Especially under challenging GNSS conditions, this is a crucial problem. One common approach is to minimize these effects by longer observation durations, which in turn increases the effort in time and cost. In this paper, an algorithm is proposed that provides accurate georeferencing results, even under challenging measurement conditions and short observation durations. It iteratively improves the georeferencing accuracy by determining and applying obstruction adaptive elevation masks to the GNSS observations. The algorithm is tested and assessed using the data of a field test. It is demonstrated that after only 5 minutes observation duration, the ground control point coordinates can be estimated with an accuracy of 1 to 2 cm, independent from the GNSS measurement conditions. Initial states of the elevation masks are determined from a point cloud that is georeferenced using coordinates from a single point positioning solution, enhanced by a RAIM-FDE approach. Afterwards, the coordinates are estimated in a weighted least-squares baseline solution and both, the elevation masks and the coordinate estimation, are iteratively improved. Besides the significant reduction of measurement time, the proposed algorithm allows for increasing the amount of ground control points and can be applied to other direct or indirect GNSS-based georeferencing approaches.

Keywords: GNSS, NLOS reception, TLS, georeferencing, obstruction adaptive elevation masks

***Corresponding author: Florian Zimmermann,** Institute of Geodesy and Geoinformation, University of Bonn, Nußallee 17, 53115, Bonn, Germany, e-mail: f.zimmermann@igg.uni-bonn.de
Christoph Holst, Lasse Klingbeil, Heiner Kuhlmann, Institute of Geodesy and Geoinformation, University of Bonn, Nußallee 17, 53115, Bonn, Germany, e-mails: c.holst@igg.uni-bonn.de, l.klingbeil@igg.uni-bonn.de, heiner.kuhlmann@uni-bonn.de

1 Motivation

In the last years, terrestrial laser scanners (TLS) became a standard tool in the geodetic community. Since they can efficiently provide dense and accurate 3D point clouds of objects, they are used in various fields of applications. TLS are commonly used for as-built surveys of buildings, industrial facilities or historical monuments [16] and their use in deformation monitoring and engineering surveying applications is constantly increasing [9, 10]. Since in most cases scans from several positions are performed to capture the complete area of interest, the single point clouds need to be combined during the so called scan registration. A further processing step that is required in many applications is the transformation to a reference coordinate system. After the georeferencing, e. g., global 3D-building models can be derived [18] or reference values and objects for mobile mapping systems can be provided [3, 6, 11].

The process of georeferencing describes the transformation between a local and a global coordinate frame. In the context of this paper, we are dealing with TLS point clouds that are determined from distance and horizontal and vertical angular measurements in the local scanner frame (s-frame). The transformation to a global coordinate frame, like e. g., WGS84/ITRF (e-frame), which is commonly accomplished by a 3D-Helmert transformation [22]. Under the assumption of the equality of the scale in both frames, the transformation requires six transformation parameters, three translations (t_x, t_y, t_z) and three rotations (α, β, γ) and is represented by the transformation equation

$$\begin{bmatrix} x_e \\ y_e \\ z_e \end{bmatrix} = \begin{bmatrix} t_x \\ t_y \\ t_z \end{bmatrix} + \mathbf{R}_s^e(\alpha, \beta, \gamma) \cdot \begin{bmatrix} x_s \\ y_s \\ z_s \end{bmatrix}, \tag{1}$$

where $\mathbf{R}_s^e$ denotes the combined rotation matrix around the x-, y- and z-axis, respectively [8].

The georeferencing can be performed in direct or indirect mode [17]. In the direct georeferencing, the scanner position needs to be known or measured in the global coordinate frame. Furthermore, a backsight target with known coordinates might be used to determine the orientation

parameters [1]. Another option is to equip the TLS with a GNSS antenna to directly determine the scanner position. In case the GNSS antenna is mounted eccentrically to the vertical rotation axis, the transformation parameters can be estimated during the rotation of the TLS and the backsight target can be neglected [14].

Indirect georeferencing incorporates a sufficient number of scanning targets on ground control points (GCP) with known coordinates in both coordinate frames to estimate the transformation parameters. Alternatively, the georeferencing can be realized using already georeferenced surfaces or building models [18].

However, since in most cases the position of the GCP or the scanner positions are measured with GNSS to establish the connection to the global coordinate frame, the accuracy of the georeferencing directly depends on the accuracy of the GNSS positioning solution. Especially under challenging GNSS measurement conditions, like e. g., in urban environments, station-dependent effects, such as non-line-of-sight reception (NLOS), signal diffraction and far-field multipath can deteriorate the accuracy of the GNSS positioning solution. Although these effects are often summarized as multipath, it is necessary to distinguish between the different effects. NLOS reception occurs if the direct line-of-sight between the receiver antenna and the satellite is blocked and only the reflected signal reaches the antenna. Signal diffraction is also a type of NLOS reception, but in this case, the signal is diffracted at the edge of an obstacle and is bended into the shadowing zone of the obstruction source. In both cases, the ranging error equals the additional path length [20]. Finally, far-field multipath describes the interference of direct and indirect signals. Here, the observation error is limited to one quarter of the respective wavelength [8]. In Figure 1, the different effects are shown schematically.

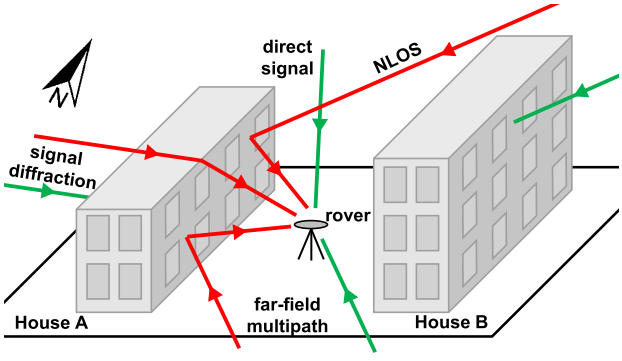

Figure 1: Site-dependent GNSS effects. The green arrows represent the direct signal paths and the red arrows represent the reflected or diffracted signals.

The easiest way to minimize the influence of these effects is locating the ground control points in areas where good GNSS measurement conditions can be found. That means areas with a nearly free horizon and no multipath emitting surfaces. Unfortunately, this cannot always be achieved. One of the most common approaches is to perform GNSS measurements over long duration, since especially the far-field multipath effect can be minimized by averaging, due to the periodic characteristic of the effect [19]. Nevertheless, besides increasing the time and cost consumption, this approach can require additional GNSS equipment, if several GCPs have to be measured with GNSS at the same time.

NLOS reception and signal diffraction can be mitigated by ray-tracing approaches [13]. Therefore, the antenna environment and the characteristics of all possible reflectors, as well as antenna and receiver properties, need to be known precisely. Thus, this approach implies non-negligible effort for additional measurements and investigations. In urban positioning, NLOS effects are a well-known problem and often impede an accurate and reliable positioning solution. Since 3D city models are becoming readily available, they can be used to identify and exclude signals that are subject to NLOS reception [5, 15].

In [25], obstruction adaptive elevation masks (OAEM) are presented and used to efficiently increase the accuracy of the GNSS positioning solution, even under challenging GNSS conditions. Here, the OAEMs are derived from georeferenced TLS point clouds and eliminate signals which are subject to NLOS reception or signal diffraction from the position estimation process. Using this approach for georeferencing TLS point clouds is a typical chicken-egg problem. On the one hand, accurately georeferenced point clouds are needed to exploit the full potential of OAEMs and to provide accurate positioning solutions in GNSS-denied environments. On the other hand, the accurate georeferencing of TLS point clouds requires accurate GNSS position solutions, which are difficult to achieve, especially under these challenging GNSS measurement conditions.

In this paper, we present an algorithm, which iteratively performs indirect georeferencing of the TLS point cloud and the OAEM determination in two consecutive processing steps. The integration of OAEMs into the georeferencing process allows for a considerable reduction of the required measuring effort, without a significant loss of accuracy. We analyze the performance of the proposed approach considering three main aspects:

(1) the density of the TLS point cloud and its impact on the accuracy of the OAEM determination
(2) the accuracy of the initial GCP positions

(3) short observation duration with different satellite constellations.

Section 2 briefly introduces OAEMs and in section 3, the newly proposed iterative OAEM determination and georeferencing algorithm is explained in detail. In section 4, the field test and the data basis are presented. Furthermore, the determination of a reference solution for validation purposes is described. In relation to the aforementioned aspects, a comprehensive and profound evaluation of the findings is presented in section 5 and a summary and an outlook on further investigations is given in section 6.

2 Introduction to Obstruction Adaptive Elevation Masks (OAEM)

Obstruction adaptive elevation masks are derived from georeferenced point clouds and are used for the mitigation of non-line-of-sight (NLOS) reception, signal diffraction and possible signal distortions induced by vegetation. By computing the azimuth and elevation angle for every point in relation to the GNSS antenna and assigning the values to an azimuthal grid with a predefined cell width, the points with the highest elevation value in a certain direction can be identified and used to build the OAEM. In order to incorporate the uncertainty of the antenna position into the determination process, the uncertainty is propagated onto the identified elevation angles in an adjustment step and afterwards, the propagated uncertainty is added to the respective OAEM value. Finally, the OAEMs can be used to identify satellite signals that are subject to NLOS reception or signal diffraction. By excluding them from the position determination process both, the accuracy and the ambiguity fixing rate, can be efficiently increased [25]. It should be noted that far-field multipath effects are not mitigated by the OAEMs.

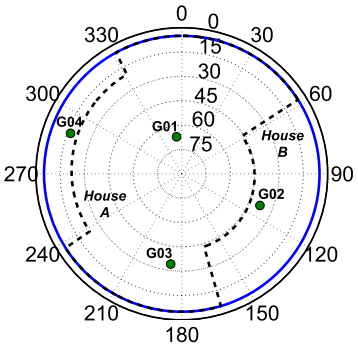

Figure 2: Obstruction Adaptive Elevation Mask (OAEM) for the artificial scenario given in Figure 1. The blue line denotes a standard 5° elevation mask. The black dashed line represents the OAEM.

Figure 2 shows a simplified OAEM for the artificial scenario depicted in Figure 1. After modifying the standard elevation mask of 5° (blue line), the satellite elevation angles are compared to the OAEM (black dashed line) in every observation epoch. The signals of the satellites *G02* and *G04* could be identified as being subject to signal diffraction or NLOS reception respectively and, thus, would be excluded from the observation data set.

3 Iterative georeferencing and OAEM determination

By integrating the OAEM determination into the georeferencing process, we aim at reducing the GNSS observation duration, while still providing accurate georeferencing results. Therefore, and especially in case of challenging GNSS measurement conditions, it is necessary to improve the GNSS-based GCP coordinate estimation accuracy. Figure 3 shows the iterative georeferencing and OAEM determination algorithm schematically, which is completely implemented in Matlab®.

In a first step, the positions of the GCPs $\hat{\mathbf{X}}^e$ are determined in a weighted-least-squares-adjustment (WLS) using the GPS code observations. To optimize the single point positioning solution (SPP), a Receiver Autonomous Integrity Monitoring approach, including fault detection and exclusion (RAIM-FDE), is applied. Afterwards, the transformation parameters from the s-frame to the e-frame ($\mathbf{t}_s^e, \mathbf{R}_s^e$) are estimated in a Gauss-Helmert-Model (GHM) using the coordinates of the ground control points in the respective coordinate frames ($\mathbf{X}_s$, $\hat{\mathbf{X}}^e$). Based on the point cloud georeferenced with these points and the estimates of $\hat{\mathbf{X}}^e$, the OAEMs are determined following the method described in section 2. Afterwards, a WLS baseline solution is carried out, where GPS phase observations that are subject to NLOS reception are identified and excluded by the OAEM. Finally, the new estimates of the GCPs ($\tilde{\mathbf{X}}^e$) are compared to the initial values $\hat{\mathbf{X}}^e$. If the difference exceeds a predefined threshold T, the estimates of $\tilde{\mathbf{X}}^e$ are used as new starting values for the georeferencing step. Otherwise, the iterative algorithm converged.

Although a GPS-only solution is carried out during the optimized SPP and WLS baseline estimation, the algorithm can be augmented with satellite signals from other GNSS systems. However, it should be noted that while satellite geometry and integrity could benefit from other

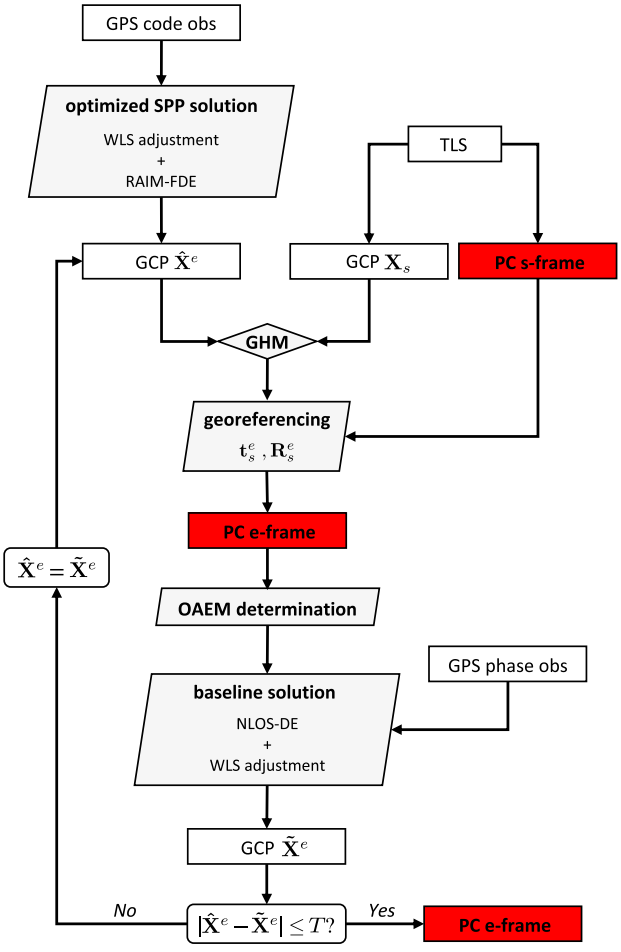

Figure 3: Schematical description of the iterative OAEM determination and georeferencing algorithm (PC = point cloud).

GNSS systems, it is likely that the number of signals that are subject to NLOS reception or signal diffraction will increase as well.

In the following paragraphs the single computation steps are described in detail.

Optimized SPP solution

In order to generate starting values for the proposed iterative OAEM determination and georeferencing algorithm, a SPP solution including a RAIM-FDE algorithm is carried out.

The observation equation of a GPS code observation ρ is given by

$$\rho = r + c \cdot \delta t_R + \epsilon \tag{2}$$

where r denotes the geometrical distance between the receiver R and the satellite, δt_R denotes the receiver clock error multiplied by the speed of light c and ϵ contains all systematic observation errors and the observation noise [4].

For every visible satellite in one observation epoch, the observation equation (2) is formulated. After linearization at approximate parameter values $\mathbf{x}_0 = [x_0, y_0, z_0, \delta t_0]^T$, the functional model of the WLS is given by

$$\begin{aligned} \Delta\hat{\mathbf{x}} &= \left(\mathbf{A}^T\mathbf{P}\mathbf{A}\right)^{-1}\mathbf{A}^T\mathbf{P}\Delta\mathbf{l} \\ \hat{\mathbf{x}} &= \mathbf{x}_0 + \Delta\hat{\mathbf{x}} \end{aligned} \tag{3}$$

where $\Delta\hat{\mathbf{x}}$ are the parameter updates to the approximate values, $\mathbf{A}$ contains the partial derivatives of ρ with respect to the parameters, $\mathbf{P}$ is the weight matrix containing satellite elevation dependent weights and $\Delta\mathbf{l}$ are the differences between the current and predicted observations from (2). The covariance matrix of the parameters $\hat{\mathbf{x}}$ is given by

$$\mathbf{\Sigma}_{\hat{\mathbf{x}}\hat{\mathbf{x}}} = \mathbf{\Sigma}_{\Delta\hat{\mathbf{x}}\Delta\hat{\mathbf{x}}} = \sigma_0^2\left(\mathbf{A}^T\mathbf{P}\mathbf{A}\right)^{-1} \tag{4}$$

with σ_0^2 denoting the a-priori variance factor, and the observation residuals can be computed from

$$\mathbf{v} = \mathbf{l} - \mathbf{A}\hat{\mathbf{x}}. \tag{5}$$

In order to optimize the estimation of the parameters $\hat{\mathbf{x}}$, a RAIM-FDE algorithm is applied. Receiver Autonomous Integrity Monitoring (RAIM) techniques are used for testing the reliability of a positioning solution and are based on the consistency check of redundant observations [24]. In this case, a global test and an observation subset testing is implemented to detect and exclude faulty measurements (FDE). The test statistic τ for the global test is defined by

$$\tau = \frac{\mathbf{v}^T\mathbf{P}\mathbf{v}}{n-m} \tag{6}$$

where $n - m$ denotes the number of degrees of freedom. The test statistic τ is compared against the quantile k of the chi-square distribution

$$k = \frac{\chi^2_{1-\alpha,n-m}}{n-m} \tag{7}$$

where α is the false alarm probability, which is set to 5 %. In case of $\tau < k$, the measurements are considered as being consistent and the SPP solution is reliable. Otherwise ($\tau \geq k$), an inconsistency of the measurements is detected and an outlier among the measurements is assumed. In this case, an observation subset testing is performed. This means the set of observations is reduced by one in all possible combinations and the SPP solutions from the subsets are tested again. If a subset passes the global test, the outlier is identified and can be excluded. If no subset passes

the global test, the subset with the lowest test statistic is reduced by one observation in all combinations and tested again. It becomes obvious, that at least six pseudorange observations are needed for a FDE algorithm. Hence, this procedure is repeated until the minimum of six observations is reached. In case that no subset passed the global test, the SPP solution is declared as unreliable.

Georeferencing

At first, the six transformation parameters between the s-frame and the e-frame given in Eq. (1) are estimated in a Gauss-Helmert-Model (GHM) using the coordinates of the six control points $\mathbf{X}_s$ and $\hat{\mathbf{X}}^e$ [17]. The uncertainty of $\mathbf{X}_s$ is derived from the discrepancies of the scan registration and the uncertainty of $\hat{\mathbf{X}}^e$ is determined during the least-squares positioning solution by Eq. (4). Afterwards, the local point cloud coordinates given in the s-frame are transformed to the e-frame according to Eq. (1).

OAEM determination

Prior to the baseline solution, the OAEM for the respective rover position is determined according to the method described in section 2. In case of the OAEM determination for the SPP solution, due to the high uncertainty of this solution, the adjustment step in the algorithm is omitted in order to impede an inflating of the OAEM. In the successive iterations, the adjustment step is performed using the uncertainty of the positioning solution. After the OAEM determination, satellites that are subject to NLOS reception are detected and excluded from the observation set.

It should be noted that the determination of the OAEM in the e-frame does not require any assumptions regarding leveled laser scanners and/or usage of accurate compensators. It can be performed independent from the orientation of the s-frame. If we assume the local point cloud to be properly leveled, the elevation angles between GCP and object points are identical in both, the scanner and the global frame, and will not change during the georeferencing. Thus, the elevation angles can be determined outside the process loop in the s-frame and only the unknown corresponding azimuthal direction needs to be adjusted iteratively in the OAEM determination step.

Baseline solution

The baseline parameters $\mathbf{b} = [b_x, b_y, b_z]^T$, which represent the position of the rover relative to the master station, are estimated in a weighted least-squares adjustment. GPS-L1 and GPS-L2 code and carrier-phase observations are used and a single- and double-differencing of the observations is performed to reduce atmospheric and satellite related errors [8]. Furthermore, individual antenna calibration parameters are applied to minimize the influence of antenna related errors [23]. The parameter estimation is performed in three steps: 1) float solution, 2) integer ambiguity fixing and 3) fixed solution.

In the float solution step, the ambiguities are estimated as real numbers in the WLS adjustment. Afterwards, the ambiguities and their covariance matrix are used to fix the ambiguities to integer values using the MLAMBDA method [2]. The result of the ambiguity fixing is validated by a ratio test [21]. Here, the squared norm of the residuals of the best set of ambiguities (R_1) and the second best set of ambiguities (R_2) are compared. If the quotient R_2/R_1 exceeds a predefined threshold, the ambiguity fixing is accepted. In the last step, the fixed solution, the final baseline parameters are estimated after the fixed ambiguities are added to the observations and are eliminated from the parameter vector.

After the estimation of the baseline parameters, the absolute coordinate of the control point is determined by adding the baseline vector to the coordinate of the master station.

4 Field test and reference solution

The field test was performed in the area of a new build university campus in Bonn that shall be used as a testing site of in-house developed Mobile-Mapping-Systems, as presented, e. g., in [7]. To assess the mapping results of these systems, a cm-accurate georeferenced point cloud of the area has to be provided. In section 4.1, the related measurement concept and the data basis is presented. For evaluation purposes, a reference solution for both, the GCP and the point cloud, is needed. The determination of this ground truth data is described in section 4.2.

4.1 Measurement concept

The whole area of the university campus has a dimension of approximately 120 × 175 meters and was captured with a Leica ScanStation P20 panoramic laser scanner from 14 positions. Afterwards, a target-based registration of the single scans was performed in the software package Cyclone,[1] leading to a dense point cloud of approximately 3.5

1 https://leica-geosystems.com/de-de/products/laser-scanners/software/leica-cyclone

billion points. Furthermore, for an observation duration of at least six hours, six scan target positions (hereafter referred to as *Ground Control Points - GCP*) were equipped with Leica AS10 and Leica AX1202GG antennas in combination with Leica GS25 and Leica GPS1200 receivers. It should be noted that prior to the field test, all used GNSS antennas were individually calibrated in the anechoic chamber of the university of Bonn [23].

The six GCP were uniformly distributed over the area and provide different qualities of GNSS measurement conditions. Based on visual inspections, an a-priori assessment of the GCP in relation to the antenna surrounding and the expectable measurement quality is given in Table 1.

Table 1: A-priori GCP assessment.

GNSS conditions	Antenna surrounding
P1 good	distant buildings in northern direction obstructions only at low elevations
P2 medium	close building in northern direction obstructions only at low elevations
P3 good	distant building in eastern direction obstructions only at low elevations
P4 bad	very close building in eastern direction close buildings and vegetation in northern direction
P5 bad	surrounded by buildings and vegetation
P6 bad	surrounded by close buildings vegetation in northern and eastern direction

As described in section 1, the absolute accuracy of the georeferencing depends on the absolute accuracy of the master station. Since in the surrounding area of the campus no points with accurately known coordinates were available, the Geodetic Post-Processing Service (GPPS) of the German Satellite-Positioning-Service (SAPOS)[2] was used to generate GNSS observations of a virtual reference station (VRS) for the respective observation duration. In order to establish baselines of similar lengths, the VRS was located in the middle of the test area, defined by the mean value of the SPP solution of the six GNSS stations. In Figure 4, the test area including the GNSS stations and the point cloud of the campus is shown.

In order to assess the effectiveness of the proposed algorithm for short time observations, the original GNSS

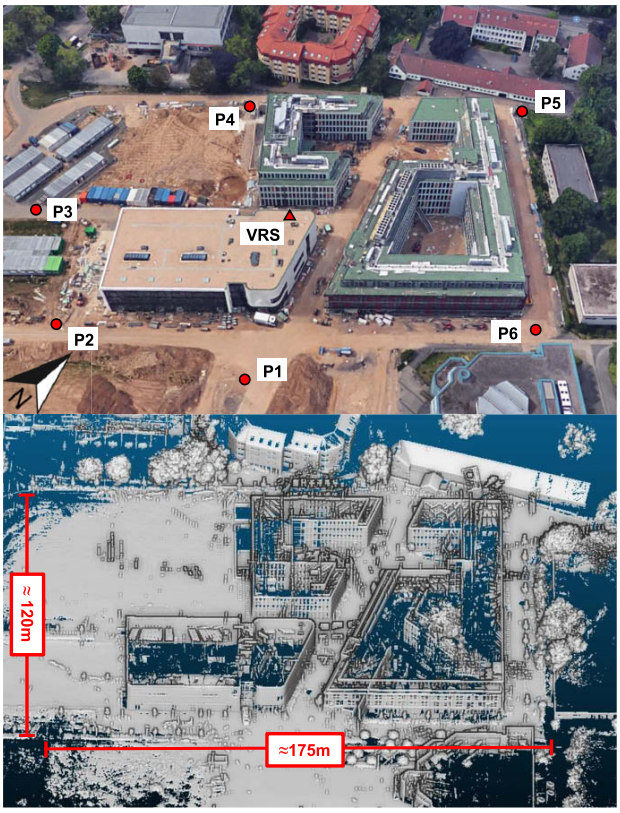

Figure 4: Test area campus Bonn. Top: Aerial image including the positions of the GNSS stations P1 to P6 and the position of the virtual reference station (VRS)(©GoogleEarth 2018). Bottom: Screenshot of point cloud.

data sets are split into five subsets of 5 minutes duration (S1 to S5) that are equally distributed over the whole observation duration. In addition to the observation duration, this allows for an assessment of the algorithm performance under different satellite constellations. Furthermore, since the total number of points of the point cloud is too big to be efficiently processed in Matlab®, the point cloud is sampled down for predefined minimum point-to-point distances (P2P) of 5 cm, 10 cm, 20 cm and 50 cm. Table 2 gives an overview of the TLS and GPS data sets.

4.2 Reference solution

The results of the proposed iterative OAEM determination and georeferencing algorithm should be validated against a reference solution for the coordinates of the ground control points and the georeferenced point cloud. For this purpose, the data sets were processed in a 'traditional' two-step procedure as described below.

In the first step, the long-time GPS observations $G_{P1\text{-}P6,orig}$ were processed in a batch LS solution to mini-

2 https://www.sapos.de

Table 2: Overview of TLS and GPS data sets.

TLS point clouds		
$\mathbf{PC_5}$	P2P distance 5 cm	≈ 174 million pts
$\mathbf{PC_{10}}$	P2P distance 10 cm	≈ 57 million pts
$\mathbf{PC_{20}}$	P2P distance 20 cm	≈ 21 million pts
$\mathbf{PC_{30}}$	P2P distance 50 cm	≈ 2 million pts
GPS data sets		
$\mathbf{G_{P1\text{-}P6,orig}}$	raw observations	6–8 hours duration
$\mathbf{G_{P1\text{-}P6,S1}}$	raw observations	5 minutes duration
⋮	⋮	⋮
$\mathbf{G_{P1\text{-}P6,S5}}$	raw observations	5 minutes duration

mize far-field multipath effects. In order to provide a reference solution that is independent from the implemented GPS data processing described in section 3, the control point coordinates were determined using Leica Infinity[3] as a standard commercial GNSS post-processing software package. The VRS was used as the master station and the points P1 to P6 as rover stations respectively. Besides individual antenna calibrations, a standard ionosphere model and the Hopfield troposphere model were applied. For all stations, the elevation mask was set to 5°. Since possible correlations of the observations are not taken into account, Leica Infinity does not provide realistic values for the uncertainty of the estimated parameters. Therefore, due to the long observation duration and the used equipment, an accuracy at the lower millimeter level is assumed for the determined baseline parameters.

In the second step, the estimated coordinates were used to perform the georeferencing of the TLS point cloud PC_5 in Cyclone and the integrated georeferencing algorithm.

As demonstrated in [25], OAEMs can be used to efficiently improve the accuracy of the positioning solution by mitigating NLOS reception and signal reflection. Thus, the 'traditional' procedure was extended by the determination and application of OAEMs. Following the algorithm described in section 2, the OAEMs were determined from the georeferenced point cloud PC_5 for the coordinates of the points P1 to P6. Afterwards, satellite signals that are subject to NLOS reception or signal diffraction were identified and excluded and the RINEX files were rewritten. Finally, the reference solution for the GCPs ($\mathbf{X_{ref}}$) was determined by reprocessing the modified observation files using the same parameter settings as described before. By applying an error propagation to the transformation process, the GCP accuracies σ_{GCP} are determined, yielding values of approximately 3 mm for all points. The reference point cloud ($\mathbf{PC_{5,ref}}$) was provided after the repetition of the georeferencing in Cyclone using $\mathbf{X_{ref}}$. According to Table 2, the reference point clouds for the other point-to-point distances where generated by downsampling $\mathbf{PC_{5,ref}}$ to the respective values.

5 Evaluation

The findings of the proposed algorithm are evaluated according to the three main aspects of the paper (see section 1). In section 5.1, the influence of the density of the point cloud, specified by different minimum P2P distances, on the accuracy of the OAEM determination is analyzed. In section 5.2, the effectiveness of the implemented RAIM-FDE algorithm for determining the initial GCP coordinates is investigated and in section 5.3, the results of the combined iterative georeferencing and OAEM determination algorithm are presented and evaluated for short observation durations.

5.1 Influence of P2P distances on OAEM determination

In principle, OAEMs represent the borders of all surrounding obstruction sources, as they are seen from the antenna's perspective. Since the OAEMs are determined from TLS point clouds, the density of these point clouds has a direct impact on the accuracy of this representation. Generally speaking, the higher the point cloud density, the higher the level of detail and, thus, the better the accuracy of the OAEM determination. However, in our case, the original point cloud of the university campus is too big to be processed in Matlab®, especially in an iterative algorithm. Hence, the density of the point cloud needs to be reduced, which is achieved by defining different minimum point-to-point distances (see Table 2).

In order to analyze the impact of this downsampling on the accuracy of the elevation masks, the OAEMs for the GCP P1 to P6 are determined according to section 2, using the GCP coordinates $\mathbf{X_{ref}}$ and the different point clouds PC_5, PC_{10}, PC_{20} and PC_{50}. Since a P2P distance of 5 cm should be small enough for a precise and complete representation of the antenna surrounding, the OAEMs determined from point cloud PC_5 serve as a reference for the accuracy analysis. In Figure 5 and 6, the differences of the OAEMs for P2P distances of 50 cm, 20 cm and 10 cm to the

3 https://leica-geosystems.com/en-sg/products/gnss-systems/software/leica-infinity

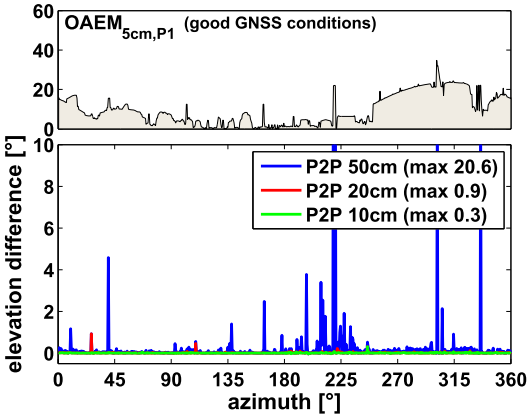

Figure 5: $OAEM_{5\,cm}$ for GCP P1 (top panel) and differences of OAEMs for P2P distances 50 cm (blue), 20 cm (red) and 10 cm (green) to $OAEM_{5\,cm}$ (bottom panel). Differences larger than 10° are truncated.

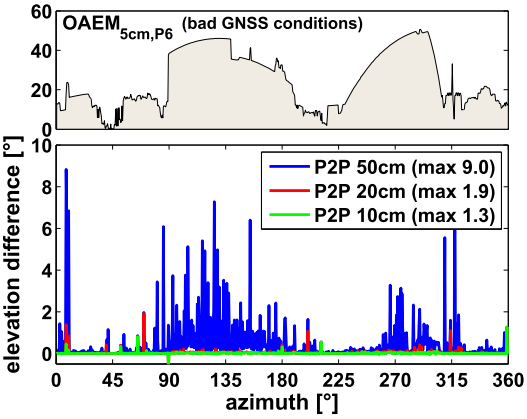

Figure 6: $OAEM_{5\,cm}$ for GCP P6 (top panel) and differences of OAEMs for P2P distances 50 cm (blue), 20 cm (red) and 10 cm (green) to $OAEM_{5\,cm}$ (bottom panel).

reference OAEM are shown for the GCP P1 and P6 exemplarily. The differences for the GCP P2 to P5 are in the same order of magnitude and are not shown for reasons of clarity.

Both graphs reveal that a P2P distance of 50 cm leads to the highest differences at both GCP. For GCP P1, several higher peaks with values up to 20.6° occur for example around azimuth values of approximately 225°, 300° and 335°. Relating these peaks to the OAEM shown in the top panel reveals that in these areas thin objects, such as lightning conductors or other kinds of masts, are present. Due to the minimum P2P distance of 50 cm, these objects are not completely represented by the point cloud any more and, thus, are the reason for the higher differences. The same holds for the differences around an azimuth value of 10° for GCP P6 (see Figure 6). Moreover, between azimuth values of 90° and 180° and 270° and 315° a lot of high differences can be found. These differences can be related to the high buildings surrounding GCP P6. After the downsampling of the point cloud, the roof edges cannot be extracted sharp enough by the OAEM algorithm, leading to differences up to 9°.

In contrast, at both GCP, the differences of the OAEM for a P2P distance of 20 cm does not exceed values of 0.9° and 1.9° respectively. These values only appear occasionally and cannot directly be related to the antenna surrounding. However, the OAEM for the P2P distance of 10 cm only slightly improves the accuracy of the OAEM determination in both cases.

To analyze the impact of the different P2P distances on the NLOS detection, the respective OAEMs are applied to the datasets $\mathbf{G_{P1\text{-}P6,orig}}$ (see Table 2). Afterwards, the number of signals that are identified as being subject to NLOS reception are compared to the respective number derived from $OAEM_{5\,cm}$. In Figure 7, the number of non-detected signals is shown for each GCP.

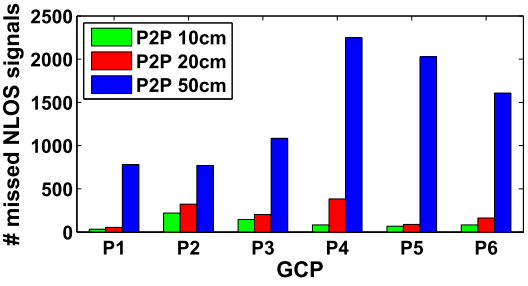

Figure 7: Number of NLOS signals that are not detected by OAEMs derived from P2P distances of 50 cm (blue), 20 cm (red) and 10 cm (green).

For all GCP, a P2P distance of 50 cm leads to a significantly higher number of non-detected NLOS signals, compared to the OAEMs derived from P2P distances of 10 cm and 20 cm. For example at GCP P5, the number increases by a factor of nearly 10. In contrast, the difference of the number of non-detected signals between P2P distances of 10 cm and 20 cm is much smaller.

Taking both into account, the elevation differences and the success rate in NLOS detection, the point cloud PC_{20} can be denoted as the best compromise between total number of points and OAEM accuracy for this scenario. Therefore, it is used in the proposed algorithm. However, for other scenarios, an adaption of the minimum P2P distance according to the characteristic of the antenna surrounding could be necessary.

5.2 Effectiveness of RAIM-FDE algorithm

The initial coordinates of the GCP in the e-frame are determined by a SPP solution and are used for georeferencing the TLS point cloud in the first iteration of the proposed algorithm. That means the transformation parameters are estimated by minimizing the discrepancies between the e-frame and s-frame coordinates of the GCP in a free adjustment without any constraints. Hence, signals that are subject to NLOS reception not only deteriorate the accuracy of the SPP solution, they also directly influence the accuracy of the transformation parameters and, in turn, the OAEM determination. If a point cloud is georeferenced with transformation parameters that are determined from corrupted SPP solutions, in the worst case, the point cloud can be located above one or more GCPs, after it is translated and rotated into the e-frame. As a consequence, all satellites would be excluded by the resulting OAEM and a coordinate estimation for these GCPs is not possible any more. Thus, the initial SPP solution should be as accurate as possible, independent from the GNSS measurement conditions. For this purpose, a RAIM-FDE algorithm is implemented and used for the detection and exclusion of faulty observations.

In order to assess the influence of the RAIM-FDE algorithm on the accuracy of the initial position solution, the GCP coordinates after the optimized SPP solution ($\hat{\mathbf{X}}^e$) for the data sets $G_{P1\text{-}P6,S1}$ to $G_{P1\text{-}P6,S5}$ are analyzed. Therefore, the positioning error $\mathbf{\Delta X} = \mathbf{X_{ref}} - \hat{\mathbf{X}}^e$ is determined, where $\mathbf{X_{ref}}$ denotes the GCP reference solution (see section 4.2). After transforming the global coordinates to a local topocentric East-, North- and Up-frame (ENU), the horizontal and vertical position errors (HPE and VPE) are determined by

$$\begin{aligned} \mathrm{HPE} &= \sqrt{\mathbf{\Delta X}_E^2 + \mathbf{\Delta X}_N^2}, \\ \mathrm{VPE} &= \mathbf{\Delta X}_U. \end{aligned} \tag{8}$$

In accordance with the GCP assessment in section 4, due to the mostly good to medium GNSS measurement conditions at points P1 to P3, the RAIM-FDE algorithm does not influence the accuracy of the coordinate estimation at these points significantly. Hence, in Figure 8, only the horizontal and vertical position errors for the points P4 to P6 are shown. To emphasize the effectiveness of the RAIM-FDE algorithm, also the positioning errors for the SPP without RAIM (*Orig*) are shown. For a better visualization, the HPE and VPE values are color coded.

The comparison of the results demonstrates that especially the accuracy of the vertical component profits from the detection and exclusion of faulty measurements. In

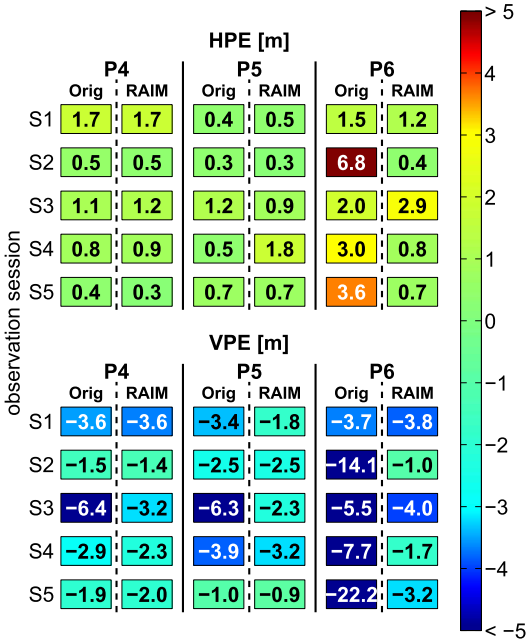

Figure 8: Horizontal (HPE) and vertical (VPE) positioning errors of the GCP P4 to P6. The original SPP solution is denoted by *Orig*, whereas the optimized SPP solution including the applied RAIM-FDE algorithm is denoted by *RAIM*.

nearly every observation session the VPE is reduced after the RAIM-FDE algorithm is applied during the SPP solution. From a geometrical point of view, this is reasonable since especially faulty signals with higher elevations are distorting the accuracy of the height component. The biggest improvements can be found for GCP P6 with approximately 13 meters in session 2 and 19 meters in session 5. In these sessions, also the HPE is considerably reduced by 6.4 meters and 2.9 meters respectively. It can be noted that for all GCP, a similar coordinate accuracy is provided by the optimized SPP solution, independent from the individual GNSS measurement conditions.

5.3 Accuracy assessment of iterative georeferencing and OAEM determination algorithm

The performance of the combined iterative georeferencing and OAEM determination algorithm is assessed by analyzing both, the accuracy of the GCP coordinates and the resulting georeferenced point clouds. In both cases, the findings are compared to the reference solution described in section 4.2.

For this purpose, the data sets $G_{P1\text{-}P6,S1}$ to $G_{P1\text{-}P6,S5}$ are processed following the algorithm described in section 3

Table 3: Horizontal (HPE) and vertical (VPE) positioning errors of the GCP P1 to P6 for observation sessions S1 to S5. The results for the original data sets are denoted as *orig* and for the proposed algorithm as *mod*. Orange colored values denote float solutions, green colored values or values without colored background denote fixed solutions.

		S1		S2		S3		S4		S5	
		HPE [m]	VPE [m]	HPE [m]	VPE [m]	HPE [m]	VPE [m]	HPE [m]	VPE [m]	HPE [m]	VPE [m]
P1	orig	0.012	0.005	0.010	-0.010	0.009	0.017	0.003	0.010	0.006	0.024
	mod	0.012	0.005	0.010	-0.010	0.009	0.017	0.003	0.010	0.006	0.024
P2	orig	0.009	0.002	0.006	0.003	0.002	-0.003	0.012	0.029	0.005	0.015
	mod	0.009	0.002	0.006	0.003	0.002	-0.003	0.012	0.029	0.005	0.015
P3	orig	0.005	0.005	0.003	-0.004	0.008	0.012	0.009	0.024	0.008	-0.009
	mod	0.005	0.005	0.003	-0.004	0.008	0.012	0.009	0.024	0.008	-0.009
P4	orig	0.003	0.020	0.009	0.000	0.044	0.476	0.014	0.036	0.567	0.066
	mod	0.004	0.018	0.011	0.015	0.003	-0.005	0.012	0.033	0.047	-0.075
P5	orig	0.089	0.011	0.001	-0.005	0.008	-0.006	0.004	-0.005	0.004	-0.023
	mod	0.011	-0.005	0.001	-0.007	0.004	-0.008	0.009	0.003	0.002	-0.015
P6	orig	0.007	-0.007	3.692	-8.508	0.768	-0.842	0.820	-3.114	8.582	-20.757
	mod	0.002	-0.007	0.006	0.006	0.010	0.004	0.007	0.016	0.019	0.012

and using the VRS as master station. The threshold T that serves as stop criterion for the iterative algorithm is set to 1 *mm* for all observation sessions. After three iterations, the algorithm converged in session *S1*, *S2* and *S4*. In sessions *S3* and *S5*, the stop criterion is reached after four iterations. Furthermore, for reasons of comparison, the same data sets are processed with the implemented baseline solution on a non-iterative basis without the modification by the OAEMs. For both cases, the horizontal and vertical positioning errors, computed according to Eq. (8), are shown in Table 3. The results for the original data sets are denoted as *orig* and for the modified data sets as *mod*. In order to emphasize the effectiveness of the proposed algorithm, some values have a colored background according to the solution type, where orange color represents float solutions and green color fixed solutions, respectively (see section 3).

The comparison of the HPE and VPE values of the various sessions and data sets shows that the GCPs P1, P2 and P3 are not affected by NLOS or diffraction. Since in none of the original data sets any of these effects are detected by the related OAEMs, the modified data sets at these GCP equal the original data sets and, therefore, the same results are achieved in both cases. After 5 minutes observation duration, the horizontal positioning errors vary in a range of 2 to 12 mm and the vertical positioning error in a range of -9 to 29 mm respectively.

In contrast, the accuracy of GCP P4 to P6 is significantly improved by the iterative algorithm. In several sessions, the ambiguities could not successfully fixed to integer values, leading to very high values of several meters in both, the HPE and the VPE. Especially at GCP P6, the baseline solution completely fails in four sessions, resulting in accuracies at the level of the related SPP solution (see Figure 8). After the data sets are iteratively modified by the proposed algorithm, the ambiguities can be fixed in all observation sessions, leading to HPE values between 1 and 19 mm and VPE values between -15 and 33 mm. Solely in observation session 5, the differences for GCP P4 exceed these ranges with values of 47 and -75 mm, which can be explained by remaining far-field multipath effects that cannot be mitigated by the proposed algorithm. Nevertheless, compared to the differences of the original data set, the HPE is reduced by 52 cm. It can be noted that independent from the antenna environment and the GNSS measurement conditions in all observation sessions, the ambiguities can successfully be fixed to integer values. After only 5 minutes observation duration, the coordinates of the GCP are estimated with mean horizontal and vertical positioning errors of 8 mm and 4 mm, respectively.

In order to assess the resulting point cloud accuracy, the georeferenced point clouds are compared to the reference solution by computing point to point (P2P) differences. Since the point cloud is not altered by the proposed approach, a direct comparison is possible and advanced methods, like e. g. M3CM2 [12], are not necessary. In Figure 9, histograms for the norm of the P2P differences are shown for sessions *S1*, *S3* and *S5* exemplarily.

In the GCP coordinate results of the original data sets, one can find different magnitudes of HPE and VPE values

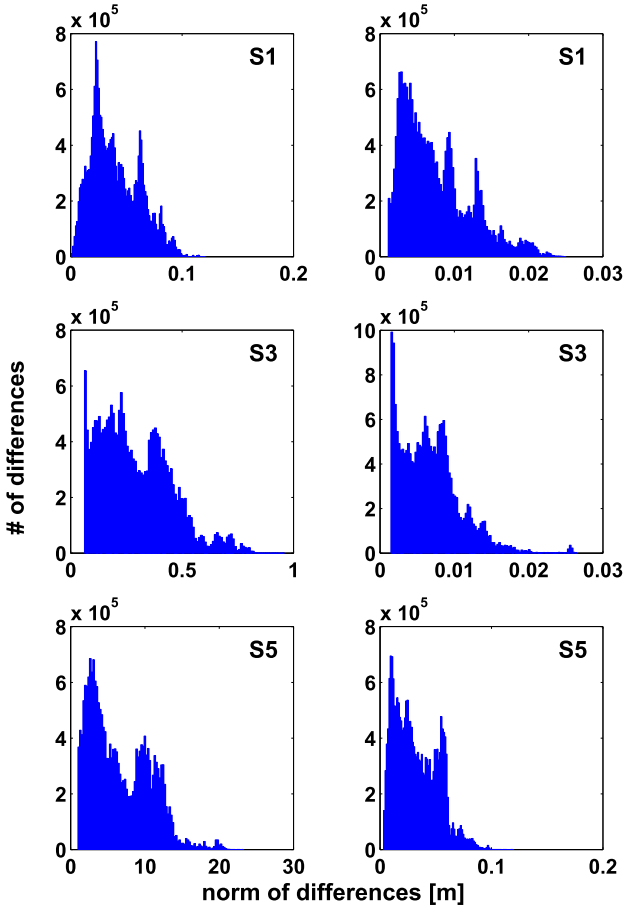

Figure 9: Histograms of the norm of the P2P differences of the point clouds determined from the original (left column) and the modified (right column) data sets. The histograms are shown for the observation sessions S1 (top), S3 (middle) and S5 (bottom).

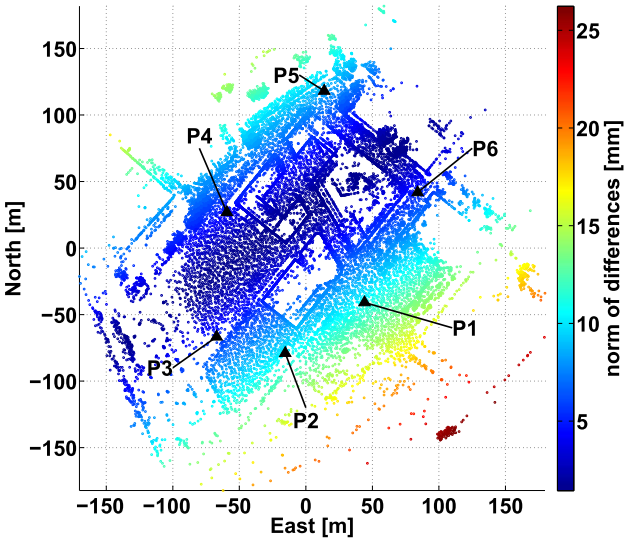

Figure 10: Top view on point cloud resulting from session S3 in a topocentric ENU system. Points are colored according to the norm of their P2P differences to the reference solution. The black triangles denote the position of the GCPs.

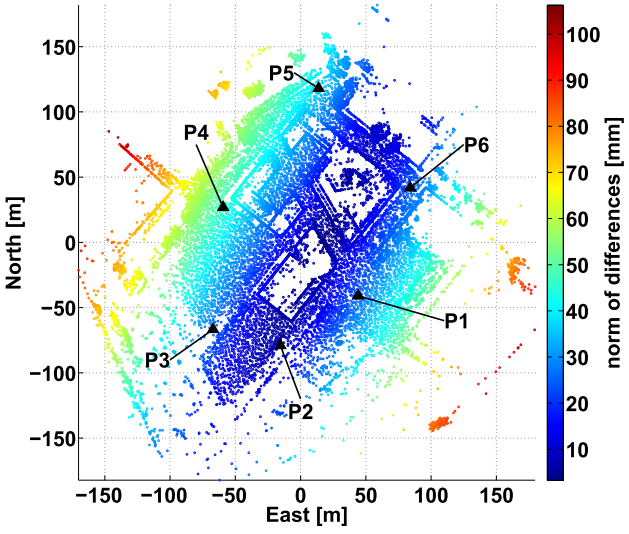

Figure 11: Top view on point cloud resulting from session S5 in a topocentric ENU system. Points are colored according to the norm of their P2P differences to the reference solution. The black triangles denote the position of the GCPs.

from some centimeters in *S1*, to a few decimeters in *S3* and up to several meters in *S5* (see Table 3). As a consequence, the norm of the P2P differences for the respective point clouds (left column in Figure 9) vary in a similar range. In contrast, the P2P differences of the point clouds that were georeferenced by the proposed algorithm do not exceed values of 3 cm in the sessions *S1* and *S3*. The same holds for the sessions *S2* and *S4* (not shown here). Only in the histogram for the session *S5*, one can find higher values of approximately 10 cm, which result from the remaining horizontal and vertical positioning errors at GCP P4 in this session (see Table 3).

In order to analyze the P2P differences in more detail, the resulting point clouds of session *S3* and *S5* are shown in Figures 10 and 11 from top view, where the points are colored according to the norm of their P2P differences to the reference solution. For reasons of clarity, the point clouds are displayed in a topocentric coordinate system instead of the global e-frame. Furthermore, Table 4 lists the differences between the transformation parameters that were estimated during the georeferencing step of the proposed algorithm and the transformation parameters of the reference solution.

In the point cloud of session S3, P2P differences higher than 15 mm can mainly be found in the north-western and

Table 4: Differences between the transformation parameters estimated during proposed algorithm and the transformation parameter from reference solution for observation sessions S1 to S5.

	translation [mm]			rotation [degree]		
	Δt_x	Δt_y	Δt_z	$\Delta\alpha$	$\Delta\beta$	$\Delta\gamma$
S1	-3	-2	-3	-0.008	0.002	-0.002
S2	-3	-3	-4	-0.002	0.003	0.001
S3	8	0	8	0.002	-0.007	-0.001
S4	9	5	14	-0.004	-0.004	0.002
S5	21	3	22	0.019	-0.019	-0.011

south-eastern direction and are increasing with the distance to the center of the GCPs. This indicates that the higher deviation in the respective rotation angle β leads to a tilting of the point cloud. For a distance of 150 m, the difference of 0.007° equals a metrical error of 18 mm. Considering this in combination with the errors of the translation parameters and the remaining rotation angles, the differences shown in Figure 10 are reasonable. The same holds for the other observation sessions. However, since mainly the three buildings in the middle of the point cloud will be used for testing and validating MMS, the higher differences in the outer area of the point cloud are not critical. Hence, for the area of interest it can be noted that the proposed algorithm provides a georeferenced point cloud with P2P differences to the reference solution smaller than 1.5 cm. The same accuracy is reached in sessions *S1*, *S2* and *S4*. Solely in session *S5*, the bigger positioning errors of GCP P4 (see Table 3) lead to higher P2P differences. For the area of interest, the highest values are between 4 cm and 5 cm and can be found in the north-western part of the buildings. It can be assumed that the glass facade of the building near the GCP leads to strong multipath effects. Since these effects are not mitigated by the OAEM approach, the GCP positioning estimation is deteriorated, and in turn, also the georeferencing suffers from these effects.

6 Conclusion and outlook

Providing accurate georeferenced TLS point clouds demands accurate GNSS coordinates for the ground control points. Especially under challenging GNSS conditions, this entails a considerable effort in time and costs, since the observation durations have to be extended in order to better cope with site-dependent effects, such as NLOS reception and far-field multipath. The proposed algorithm enables a significant reduction of the observation duration while providing point cloud accuracies of 1 to 2 cm, even under poor GNSS conditions. The algorithm rests on integrating the antenna environment into the GNSS data processing by iteratively georeferencing TLS point clouds and deriving obstruction adaptive elevation masks to mitigate NLOS reception. The initial position solutions are determined via SPP in combination with a RAIM-FDE approach, yielding to similar uncertainty levels independent from the GNSS measurement conditions. The results of the iterative algorithm are compared to a reference solution for the GCP and the point cloud that is determined following the traditional approach of long observation durations. In both cases, the differences are between a few millimeters and l to 2 cm after only 5 minutes of observation duration.

Due to this substantial reduction of observation time, the proposed algorithm allows for increasing the amount of control points. Especially for larger areas, this could improve the accuracy of the georeferencing. Moreover, the additional computational burden of the iterative position estimation and point cloud processing is negligible, compared to the time saving during the field measurements. Although the algorithm was applied to the traditional georeferencing approach in this study, in principle, it can be applied to other direct, or indirect georeferencing approaches where GNSS observations are involved.

Since only NLOS receptions and signal diffractions are mitigated by the proposed algorithm and due to the short observation durations, far-field multipath remains as critical error source. Based on the created knowledge of the antenna environment, ray-tracing approaches in combination with an analysis of the related Fresnel-zones could be used to mitigate this effect and further optimize the georeferencing accuracy. Nevertheless, further investigations are needed and this strategy is subject to current research.

Acknowledgment: We thank Erik Heinz and Tomislav Medic for their assistance during the TLS measurements.

References

[1] M. Alba and M. Scaioni, Comparison of techniques for terrestrial laser scanning data georeferencing applied to 3-D modelling of cultural heritage, *The International Archives of the Photogrammetry, Remote Sensing and Spatial Information Sciences* 36 (2007), 8.

[2] X. W. Chang, X. Yang and T. Zhou, MLAMBDA: a modified LAMBDA method for integer least-squares estimation, *Journal of Geodesy* 79 (2005), 552–565.

[3] C. Eling, L. Klingbeil, M. Wieland and H. Kuhlmann, Towards deformation monitoring with uav-based mobile mapping systems, in: *Proc., 3rd Joint Int. Symp. on Deformation Monitoring (JISDM), TU Wien, Vienna*, 2016.

[4] P. D. Groves, *Principles of GNSS, inertial, and multisensor integrated navigation systems*, Artech house, Boston, USA, 2013.
[5] P. D. Groves, Z. Jiang, M. Rudi and P. Strode, A Portfolio Approach to NLOS and Multipath Mitigation in Dense Urban Areas, in: *Proceedings of the 26th International Technical Meeting of the Satellite Division of The Institute of Navigation (ION GNSS+ 2013)*, pp. 3231–3247, Nashville, TN, USA, September 16–20, 2013.
[6] D. Hauser, C. Glennie and B. Brooks, Calibration and accuracy analysis of a low-cost mapping-grade mobile laser scanning system, *Journal of Surveying Engineering* 142 (2016), 04016011.
[7] E. Heinz, C. Eling, M. Wieland, L. Klingbeil and H. Kuhlmann, Development, calibration and evaluation of a portable and direct georeferenced laser scanning system for kinematic 3D mapping, *Journal of Applied Geodesy* 9 (2015), 227–243.
[8] B. Hofmann-Wellenhof, H. Lichtenegger and E. Wasle, *GNSS–Global Navigation Satellite Systems: GPS, GLONASS, Galileo, and more*, Springer-Verlag Wien, New York, USA, 2008.
[9] C. Holst and H. Kuhlmann, Challenges and present fields of action at laser scanner based deformation analyses, *Journal of applied geodesy* 10 (2016), 17–25.
[10] C. Holst, D. Schunck, A. Nothnagel, R. Haas, L. Wennerbäck, H. Olofsson, R. Hammargren and H. Kuhlmann, Terrestrial Laser Scanner Two-Face Measurements for Analyzing the Elevation-Dependent Deformation of the Onsala Space Observatory 20-m Radio Telescopes Main Reflector in a Bundle Adjustment, *Sensors* 17 (2017), 1833.
[11] H. Kaartinen, J. Hyyppä, A. Kukko, A. Jaakkola and H. Hyyppä, Benchmarking the performance of mobile laser scanning systems using a permanent test field, *Sensors* 12 (2012), 12814–12835.
[12] D. Lague, N. Brodu and J. Leroux, Accurate 3D comparison of complex topography with terrestrial laser scanner: Application to the Rangitikei canyon (NZ), *ISPRS Journal of Photogrammetry and Remote Sensing* 82 (2013), 10–26.
[13] L. Lau and P. Cross, Development and testing of a new ray-tracing approach to GNSS carrier-phase multipath modelling, *Journal of Geodesy* 81 (2007), 713–732.
[14] J.-A. Paffenholz, H. Alkhatib and H. Kutterer, Direct geo-referencing of a static terrestrial laser scanner, *Journal of Applied Geodesy* 4 (2010), 115–126.
[15] S. Peyraud, D. Bétaille, S. Renault, M. Ortiz, F. Mougel, D. Meizel and F. Peyret, About non-line-of-sight satellite detection and exclusion in a 3D map-aided localization algorithm, *Sensors* 13 (2013), 829–847.
[16] D. Pritchard, J. Sperner, S. Hoepner and R. Tenschert, Terrestrial laser scanning for heritage conservation: the Cologne Cathedral documentation project, *ISPRS Annals of the Photogrammetry, Remote Sensing and Spatial Information Sciences* 4 (2017), 213.
[17] Y. Reshetyuk, *Self-calibration and direct georeferencing in terrestrial laser scanning*, Ph.D. thesis, KTH, 2009.
[18] S. Schuhmacher and J. Böhm, Georeferencing of Terrestrial Laser scanner Data for Applications in Architectural Modeling, *ISPRS - International Society for Photogrammetry and Remote Sensing* XXXVI-5/W17 (2015).
[19] G. Seeber, *Satellite geodesy: foundations, methods, and applications*, Walter de Gruyter, Berlin, Boston, 2003.
[20] P. Strode and P. D. Groves, GNSS multipath detection using three-frequency signal-to-noise measurements, *GPS Solutions* 20 (2015), 1–14.
[21] S. Verhagen and P. J. G. Teunissen, New global navigation satellite system ambiguity resolution method compared to existing approaches, *Journal of Guidance, Control, and Dynamics* 29 (2006), 981–991.
[22] G. Vosselman and H.-G. Maas, *Airborne and terrestrial laser scanning*, CRC Press, 2010.
[23] P. Zeimetz and H. Kuhlmann, On the accuracy of absolute GNSS antenna calibration and the conception of a new anechoic chamber, in: *Proceedings of the FIG Working Week*, 14, p. 19, 2008.
[24] N. Zhu, J. Marais, D. Bétaille and M. Berbineau, GNSS Position Integrity in Urban Environments: A Review of Literature, *IEEE Transactions on Intelligent Transportation Systems*, (2018).
[25] F. Zimmermann, C. Eling and H. Kuhlmann, Empirical assessment of obstruction adaptive elevation masks to mitigate site-dependent effects, *GPS Solutions* 21 (2017), 1695–1706.